

ORIGINAL ARTICLE

The shallow thermal regime of Devils Hole, Death Valley National ParkMark B. Hausner,^{1,2} Kevin P. Wilson,³ D. Bailey Gaines,³ Francisco Suárez,² and Scott W. Tyler¹**Abstract**

*Devils Hole, a fracture in the carbonate aquifer underlying the Death Valley Regional Groundwater Flow system, is home to the only extant population of Devils Hole pupfish (*Cyprinodon diabolis*). Since 1995, the population of *C. diabolis* has shown an unexplained decline, and a number of hypotheses have been advanced to explain this. Here, we examine the thermal regime of Devils Hole and its influence on the pupfish population. We present a computational fluid dynamic (CFD) model of thermal convection on the shallow shelf of Devils Hole, which provides critical habitat for *C. diabolis* to spawn and forage for food. Driven by meteorological data collected at Devils Hole, the model is calibrated with temperature data recorded in the summer of 2010 and validated against temperatures observed on the shallow shelf between 1999 and 2001. The shallow shelf experiences both seasonal and diel variations in water temperature, and the model results reflect these changes. A sensitivity analysis shows that the water temperatures respond to relatively small changes in the ambient air temperature (on the order of 1 °C), and a review of local climate data shows that average annual air temperatures in the Mojave Desert have increased by up to 2 °C over the past 30 years. The CFD simulations and local climate data show that climate change may be partially responsible for the observed decline in the population of *C. diabolis* that began in 1995.*

Keywords: convection, climate change, computational fluid dynamics, Devils Hole, distributed temperature sensing

Introduction

[1] The endangered Devils Hole pupfish (*Cyprinodon diabolis*; Wales 1930) occurs only in the geothermally influenced Devils Hole ecosystem (36.42 N, 116.28 W), a groundwater-filled fracture in the carbonate aquifer underlying Ash Meadows National Wildlife Refuge in southern Nevada, USA. With a surface area of just 50 m², Devils Hole comprises a shallow shelf (average depth ~0.35 m) perched adjacent to a pool that extends more than 130 m deep. Over the past 40 years, the population

of *C. diabolis* has varied significantly, declining as groundwater mining depleted the water level in the ecosystem and then recovering in the 1970s as the water level increased (although it never reached prepumping levels) after the cessation of pumping (Andersen and Deacon 2001). In the mid-1990s, the population of *C. diabolis* began a second decline, with no immediately apparent cause (Riggs and Deacon 2002). Despite ongoing management of the ecosystem, the population remains at a reduced level, and the post-1995 population decline

¹Department of Geological Sciences and Engineering, University of Nevada, Reno, Reno, Nevada 89557 USA

²Department of Hydraulic and Environmental Engineering, Pontificia Universidad Católica de Chile, Santiago, Chile

³Death Valley National Park, Pahrump, Nevada 89048 USA

Correspondence to
Mark B. Hausner,
hausner.mark@gmail.com

remains unexplained. A number of hypotheses have been advanced to explain this decline, including inbreeding depression (Wilcox 2001), shifts in solar radiation and allochthonous inputs (Wilson and Blinn 2007), changes in sediment dynamics (Lyons 2005) and the algal community (Riggs and Deacon 2002), and the loss of a prey species from the ecosystem (Herbst and Blinn 2003). Threlhoff and Manning (2003) posited that increases in water temperature on the ecologically critical shallow shelf may be partially responsible for the population decline.

[2] The approximately 17 m² shallow shelf comprises a boulder perched between the walls of the fracture and provides the best *C. diabolis* spawning habitat in the system (Andersen and Deacon 2001), as well as a substrate for the growth of the benthic community (Wilson and Blinn 2007). With a high surface area-to-volume ratio, water temperatures on the shelf vary on both a daily and a seasonal basis. Devils Hole pupfish use the shallow shelf for spawning and foraging on a daily basis (James 1969; Baugh and Deacon 1983). Although pupfish spawn year round (Chernoff 1985), the population of *C. diabolis* normally follows a seasonal cycle (Fig. 1A), with the greatest annual increase in population observed between May and July (Riggs and Deacon 2002). Regular population surveys in Devils Hole generally count individuals 17–18 mm or larger, although smaller fish are occasionally included in the surveys when they are observed. Given the observed growth rates of *C. diabolis*, it takes 2–3 months for the fish to reach this length (James 1969); this lag time between recruitment and population surveys implies that the majority of the annual recruitment occurs in March and April.

[3] The life cycle of *Cyprinodon* spp. (or pupfishes) is strongly controlled by water temperatures, particularly during life stages associated with reproduction. In a study of Amargosa pupfish (*Cyprinodon nevadensis nevadensis*, closely related to *C. diabolis*), Shrode and Gerking (1977) delineated increasingly narrow ranges of acceptable temperatures for normal activity (12–38 °C), viable oogenesis (24–36 °C), and successful reproduction (26–30 °C), defined as >50% survival. Although spawning activity occurs year-round, the seasonal population cycle indicates that annual recruitment

of *C. diabolis* is controlled by other factors. The food web in Devils Hole is dynamic, dominated in the summer by primary productivity but changing to an allochthonous-driven system when the low winter sun and the canyon walls surrounding Devils Hole limit direct sunlight. Annual recruitment of *C. diabolis* begins in March, coinciding with the springtime increase in both allochthonous carbon input and solar radiation (which drives increased primary productivity; Wilson and Blinn 2007). After the end of April, mean water temperatures rise sharply and remain relatively constant between May and August (Fig. 1C). Whereas other environmental factors influence the viability of pupfish eggs and larvae (e.g., dissolved oxygen, hydrogen sulfide, and predation), suitable water temperatures and available food are both necessary for successful recruitment. The beginning of the annual recruitment period occurs when both allochthonous carbon inputs and primary productivity begin increasing in the spring, and this period appears to end when warm water temperatures prevent successful egg development.

[4] This article presents a computational fluid dynamic (CFD) model of thermal processes in the water column over the shallow shelf of Devils Hole and compares simulated temperatures with both historical records and temperatures observed using a fiber-optic distributed temperature sensor (DTS). The model is used to examine the circulation of water within the system and to consider the potential impacts of climate change on the ecosystem. By integrating CFD modeling with field observations, we examine the hypothesis that climate change can affect the water temperatures on the shallow shelf of Devils Hole strongly enough to affect the recruitment of *C. diabolis*. The utility of hydrodynamic modeling as a tool for evaluating changing ecosystems is demonstrated, and the model allows recommendations for future research in both Devils Hole and the American Southwest.

Methods

The Devils Hole System

[5] The ecologically critical shallow shelf of Devils Hole (Fig. 2) is approximately 5.8 m long (north–south) with a width that varies between 2 and 3 m (east–west). Because of the orientation of the shelf within the narrow

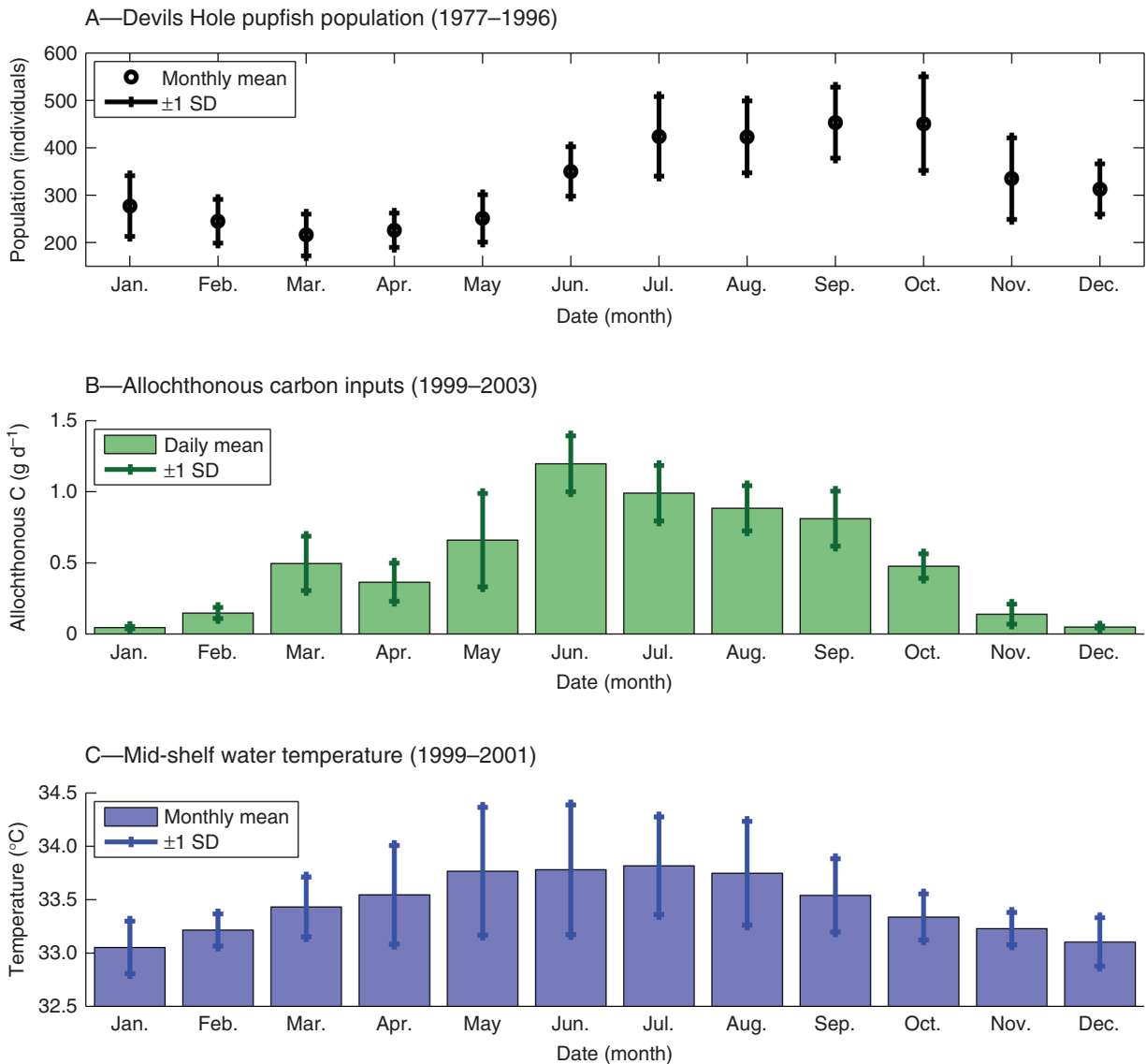


Fig. 1 Seasonal cycles in Devils Hole. A — Population surveys of Devils Hole pupfish (Riggs and Deacon 2002). B — Allochthonous carbon inputs measured between 1999 and 2003 (Wilson and Blinn 2007). C — Substrate temperature at a depth of 45 cm measured between 1999 and 2001 (Threlloff and Manning 2003).

canyon surrounding Devils Hole, direct solar exposure varies seasonally. Direct radiation strikes the water surface for up to 4.5 h d⁻¹ in June (Fig. 2A), but no direct solar exposure occurs for much of January (Wilson and Blinn 2007). The water surface is approximately 17 m below the surrounding landscape (Szabo et al. 1994), and high ridges east and west of the pool obstruct the sun for most of the day. When direct solar radiation does fall on the water surface, spatially variable exposure causes temperature gradients that in turn drive diel thermal convection on the shelf. These diel

convection cycles affect the temperatures in the water column and the substrate, where pupfish spawn and forage on a daily basis.

[6] The shallow shelf itself is a boulder perched in the aperture of the fracture. Water depth on the shallow shelf varies from a few to more than 80 cm, and the north end of the shelf drops off sharply into the deep pool. The system is subject to earth tides that induce a daily variation in water depth on the order of a few centimeters; the mean depth (averaged over both time and space) is 0.35 m. On the east side of the shelf, a gap

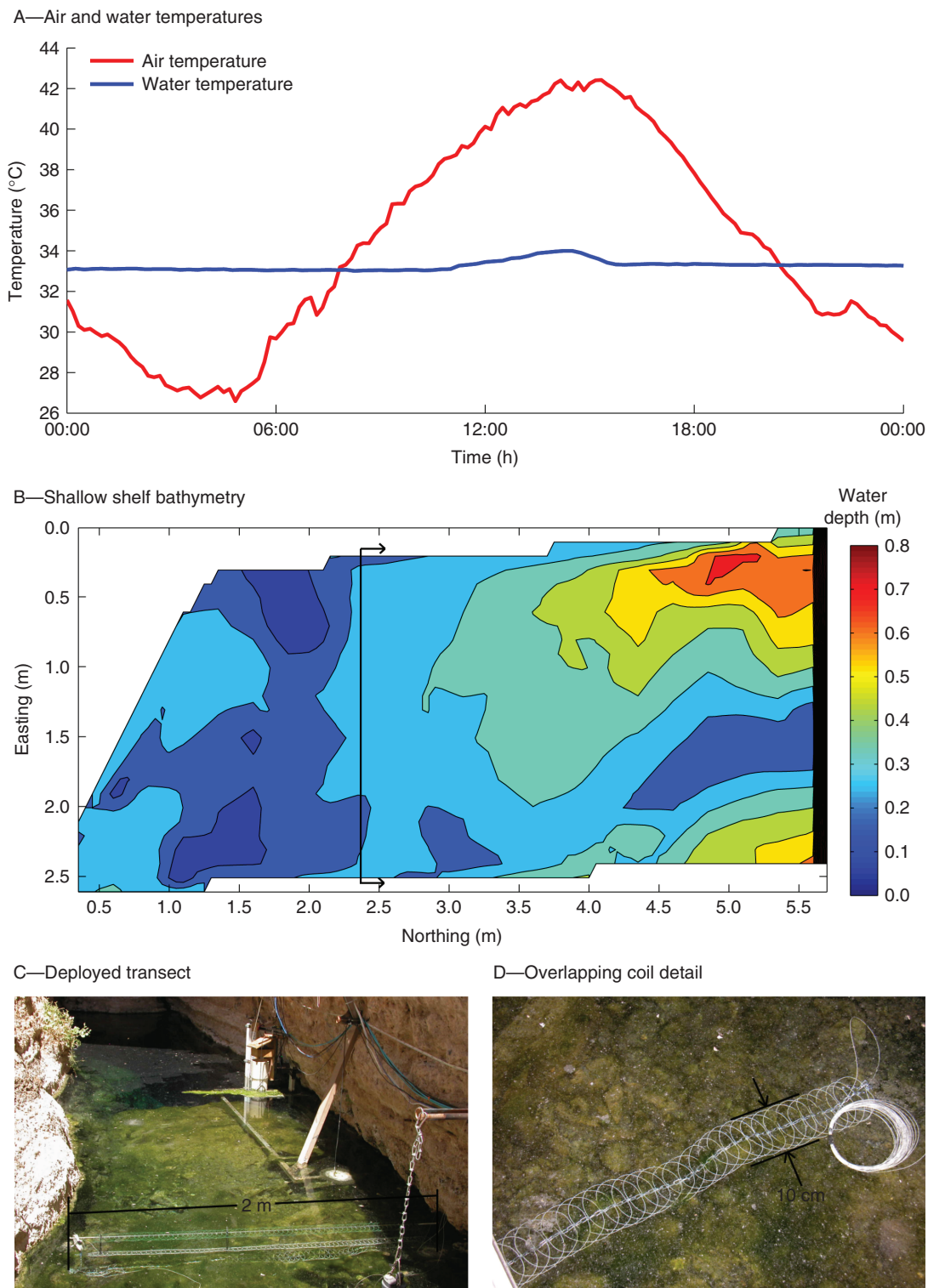


Fig. 2 The shallow shelf of Devils Hole. A — Annual cycle of air and water temperatures, 2009. B — Bathymetry of shallow shelf, 2010, with the location of the monitored cross section indicated by the black line. C — Three-transect DTS cross section deployed in Devils Hole, June 2010, that provided the basis for the modeled cross section. D — Detail of overlapping spiral configuration and chain mounting. The width of the shelf in (C) is ~2 m, and the diameter of the coiled cable in (D) is ~10 cm.

between the boulder and the fracture wall allows for fluid communication between the shelf and the deep pool below it. A layer of sediment and detritus, up to 0.3 m thick, covers the boulder, forming a sediment–water interface in which the pupfish deposit eggs and forage for food. This layer is periodically redistributed by disturbances caused by earthquakes or overland flow; Fig. 2B shows the average bathymetry of the shallow shelf during the monitored period.

Field Data Collection

[7] Field data were collected 23–24 June 2010, using a fiber-optic DTS and meteorological monitoring equipment. DTS instrumentation has been used extensively in hydrological studies (Selker et al. 2006; Westhoff et al. 2011; Suárez et al. 2011b), and DTS data have informed previous models of convection in engineered systems (Suárez et al. 2011a) and in Devils Hole (Hausner et al. 2012). The meteorological data were compared with a meteorological monitoring station operated onsite by the National Park Service. Data used included air temperature, relative humidity, incoming shortwave solar radiation (<2000 nm), and wind speed at 3 m, all collected and tabulated at 10-min intervals.

[8] A Sensornet Sentinel DTS (Sensornet Ltd., UK) was used to monitor water temperatures within a cross section of the shallow shelf. Because the thermal gradients in the short east–west direction are much greater than those along the longer north–south axis, a 0.35-m-deep by 2.15-m-wide east–west cross section was used as the basis for observation (Fig. 2C). A 900- μm , simplex tight buffered fiber-optic cable (AFL Telecommunications, USA) was placed in overlapping spirals (Fig. 2D) to provide increased spatial resolution. With this configuration, the 1-m spatial resolution provided by the DTS instrument returned the average temperature of a 10-cm \times 20-cm planar area. Three horizontal transects at different depths were monitored; 1 cm below the water surface, 20 cm below the water surface, and at the sediment–water interface, which had an average depth of 35 cm. The upper two transects comprised overlapping fiber spirals mounted on transparent polycarbonate tubing, whereas the bottom transect was mounted on a chain to contour the bottom of the shelf and

ensure good contact between the substrate and the fiber-optic cable (Fig. 2D).

[9] The DTS instrument was mounted in an air-conditioned enclosure to minimize errors due to ambient temperature fluctuation (Suárez et al. 2011a). The fiber-optic cable made multiple passes through two independently monitored calibration baths, and both ends of the fiber were connected to the instrument, allowing for double-ended observations. In double-ended DTS observations, Raman spectra scattering is observed first from one end (the forward direction) and then from the other (reverse) of the fiber-optic cable, and the two signals are combined to account for the spatially variable attenuation of light within the cable (van de Giesen et al. 2012). Data were collected in both directions along the cable using 10-s integration times and were composited into a single double-ended data set with a temporal sampling frequency of 0.05 Hz. The data were calibrated in the field using the software provided with the DTS instrument and later recalibrated according to Eqs. 1 and 2 (van de Giesen et al. 2012):

$$T\left(z, \ln \frac{P_s(z)}{P_{as}(z)}\right) = \frac{\gamma}{\ln \frac{P_s(z)}{P_{as}(z)} + C + \int_{u=0}^z \Delta\alpha(u)du}, \quad (1)$$

$$\int_{u=z}^{z+\Delta z} \Delta\alpha(u)du = \frac{1}{2} \left[\ln \frac{P_s(z+\Delta z)}{P_{as}(z+\Delta z)_{\Rightarrow}} - \ln \frac{P_s(z)}{P_{as}(z)_{\Rightarrow}} + \ln \frac{P_s(z)}{P_{as}(z)_{\Leftarrow}} - \ln \frac{P_s(z+\Delta z)}{P_{as}(z+\Delta z)_{\Leftarrow}} \right], \quad (2)$$

where T is temperature, γ and C are the calibration parameters, $P_s(z)$ and $P_{as}(z)$ are the Raman spectra Stokes and anti-Stokes power observed at the DTS instrument, respectively, z is the distance from the DTS instrument, $\Delta\alpha$ is the difference between the attenuation rates of the anti-Stokes and Stokes signals, u represents the locations on the cable for which the integral is evaluated, and the subscripts \Rightarrow and \Leftarrow indicate observations taken in the forward and reverse directions, respectively. Values of γ and C were determined and the temperatures recalculated for each 20-s integration time period of the deployment.

[10] The postdeployment calibration included an estimate of the DTS temperature uncertainties. The pre-

cision of the observations was quantified as the standard deviation of 39 observations of the same temperature (in this case, a coil of cable in the recirculated water bath used for calibration), as described by Tyler et al. (2009). The accuracy of the DTS observations was quantified as the mean bias in a second independently monitored bath that was not used in the calibration routines, as described by Hausner et al. (2011).

Computational Fluid Dynamic Modeling

[11] The CFD model of the shallow shelf was created in Fluent (Ansys, Inc., USA), a commercial software package that simultaneously solves equations for conservation of mass, momentum, and energy by using a finite volume formulation. Because the direct solar exposure is near uniform in the longer north–south direction and highly variable in the shorter east–west axis, a two-dimensional model was formulated to simulate thermal convection in the vertical plane running east–west through the shallow shelf (indicated by the section line on Fig. 2B). The cross-sectional model simulates the circulation of water in response to meteorological

drivers. A schematic of the model (Fig. 3) shows the system's physical boundaries and the energy fluxes at the boundaries and within the water column included in the model. The CFD model was calibrated against the field data collected in the summer of 2010 with the fiber-optic DTS and validated against previously recorded temperatures (Threlloff and Manning 2003).

Boundary Conditions

[12] The water level in Devils Hole is determined by its hydraulic connection to the lower carbonate aquifer, and evaporated water does not change the water depth but is instead replenished from the aquifer. The water surface was therefore modeled as a no-flow boundary. The side boundaries were also defined as impermeable walls, and the shelf bottom was modeled in two parts: a no-flow boundary extending 194 cm from the left (west) side of the model, and a vent boundary making up the remaining 20 cm of the model bottom. The bottom boundary was assumed to be flat—although the depth of water varies with location on the shallow shelf, this variation is much greater along the north–south axis

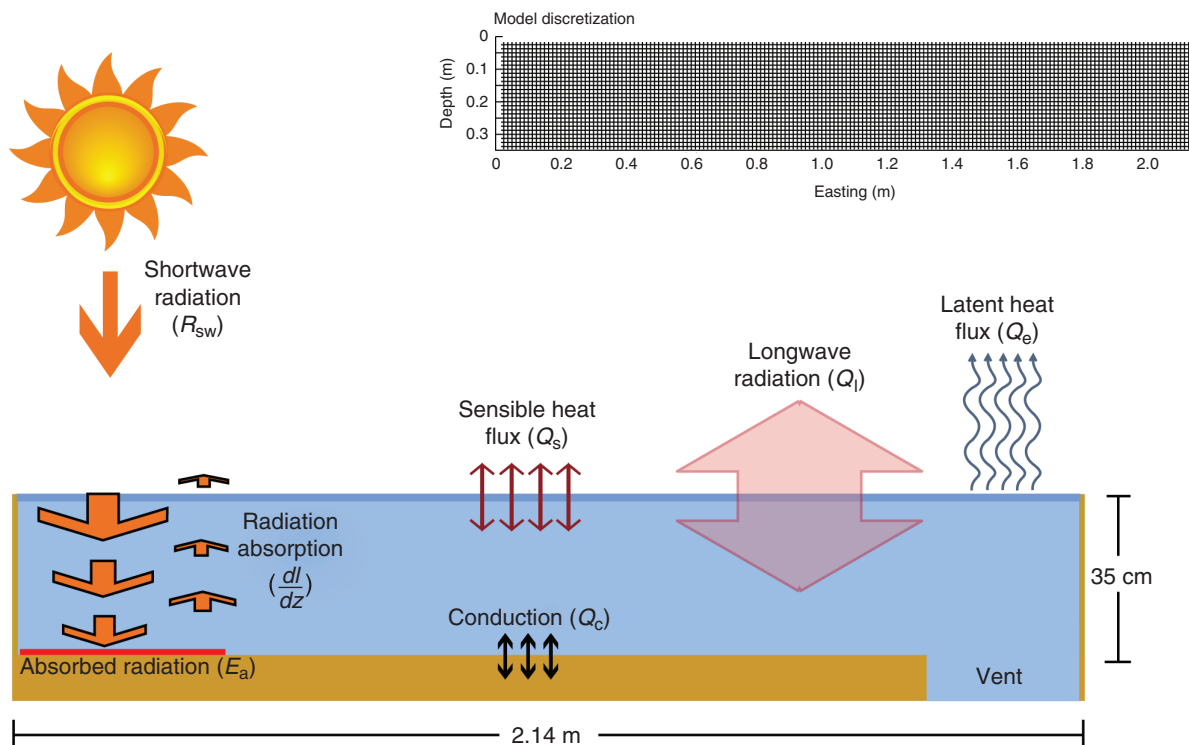


Fig. 3 Schematic of the two-dimensional computational fluid dynamic model (not to scale). The inset at the upper right shows the model discretization to scale, with each + indicating the center of a finite volume.

than along the east–west axis. The vent allowed fluid to flow in either direction normal to the boundary and reflected the hydraulic connection between the east side of the shelf and the deeper pool below the perched boulder. The water temperature on the outside of the vent was constant at 33.5 °C, reflecting the assumed constant temperature of the deep pool. There was no pressure difference between the inside and outside of the vent.

[13] The net surface energy flux (Q_{surface} in Eq. 3) included latent heat flux (Q_e), sensible heat flux (Q_s), and longwave heat flux (Q_l) and was a function of the meteorological drivers and water surface temperature:

$$Q_{\text{surface}} = Q_e + Q_s + Q_l. \quad (3)$$

The formulation of the surface heat flux is presented in Appendix A. The side walls were modeled as adiabatic boundaries. The 194-cm bottom boundary was simulated as a 50-cm-thick calcium carbonate mass with a constant temperature of 33.5 °C at its bottom (i.e., pure conduction, Q_c , occurs through the calcium carbonate boulder and the bottom of the shelf); the temperature and thermal gradients within the carbonate rock were allowed to vary in space and time, and the energy fluxes between the boundary and the water column depended on this variation. Energy fluxes at the vent were a combination of advective (depending on the simulated fluid fluxes) and conductive (based on the constant temperature of 33.5 °C) fluxes.

Absorption of Shortwave Radiation in the Water Column

[14] Shortwave radiation striking the water surface can be reflected by the surface albedo, absorbed by the surface layer of neuston (a collective term for the complex community of organisms, precipitated CaCO_3 , and other floating material accumulated on the water surface), or propagated downward into the water column and attenuated exponentially. The absorption of attenuated energy in the water column is simulated as a heat source. Simulation of this attenuation is complicated by the neuston layer that occurs on the water surface, which acts as a strongly absorbing layer. The energy absorbed by this layer (Q_n in Eq. 4) was simulated as an energy source added only to the uppermost layer of the model domain:

$$Q_n = (1 - A)R_{\text{SW}}N, \quad (4)$$

where A is the shortwave albedo of the water surface, R_{SW} is the direct shortwave radiation falling on the water surface (and varies in space and time, as described below), and N is a linear absorption coefficient ($0 < N < 1$) that quantifies the effect of the neuston layer. Values and sources for these parameters can be found in Table 1.

[15] Because the canyon walls obstruct direct solar radiation for most of the day, the shortwave radiation falling on the water surface varies on both space and time. Direct shortwave insolation at an east–west position x (m) is either 0 or the observed shortwave

Table 1 Model parameters used in the computational fluid dynamic model of Devils Hole.

Parameter	Value	Units	Description	Source
A	0.08	Dimensionless	Shortwave albedo at the water surface	Henderson-Sellers 1986
ρ_{air}	1.2	kg m^{-3}	Density of air	Incropera et al. 2007
θ	0.6	Dimensionless	Fraction of sky with an unobstructed view to the sky	Observed
T_r	303.15	K	Temperature of canyon walls	Mean daily air temperature (observed)
R	0.476	Dimensionless	Reflectivity of shelf substrate	Calibrated
N	0.550	Dimensionless	Neuston layer	Calibrated
$Atten$	1.772	m^{-1}	Attenuation rate of visible and ultraviolet light	Calibrated
$Wind$	0.356	Dimensionless	Scaling parameter for in-canyon wind speed	Calibrated
$Depth$	0.35	m	Depth of simulated water column	Measured
t_0	12,600	s	Time of first exposure to direct sunlight on westernmost edge of shelf	Observed
t_f	25,050	s	Time of last exposure to direct sunlight on easternmost edge of shelf	Observed
P_{air}	92,953	Pa	Air pressure at the water surface	Estimated
C	0.1	Dimensionless	Cloud cover parameter	Estimated

radiation:

$$R_{\text{SW}}(x, t) = \begin{cases} 0, & t < t_0(x), \\ R_{\text{SW_obs}}, & t_0(x) \leq t \leq t_f(x), \\ 0, & t > t_f(x), \end{cases} \quad (5)$$

where $t_0(x)$ is the time of first direct exposure at position x and $t_f(x)$ is the time of final exposure at position x . Both $t_0(x)$ and $t_f(x)$ were tabulated based on field observations of solar exposure.

[16] The shortwave radiation that passes through the neuston layer into the water column is attenuated according to the Beer–Lambert law. Because attenuation rates differ across the optical spectrum, the total shortwave radiation is divided into seven component spectra with individual attenuation rates (Branco and Torgersen 2009). The reflecting model considers absorption resulting from both the downward propagation of incident radiation and the upward propagation of reflected radiation. The downward irradiance $I(z)$ at any depth z in the water column is given by

$$I(z) = I_0(1 - A) \sum_{n=1}^7 f_n \exp(-\alpha_n z), \quad (6)$$

where I_0 is the incident irradiance on the water surface, f_n is the fraction of shortwave radiation occurring in component spectrum n , and α_n is the attenuation rate for that component spectrum (Table 2). Upward reflected irradiance (I') was calculated similarly:

$$I'(z) = I'_0 \sum_{n=1}^7 f'_n \exp(-\alpha_n z'), \quad (7)$$

$$I'_0 = I_0(1 - A)R \sum_{n=1}^7 f_n \exp(-\alpha_n z_{\text{max}}), \quad (8)$$

where I'_0 is the total irradiance reflected from the bottom of the water column (Eq. 8), f'_n is the fraction of this reflected irradiance occurring in component spectrum n (different from f_n in Eq. 6), and z' is the vertical distance from the bottom to depth z . In Eq. 8, R is the reflectivity of the substrate, and z_{max} is the total depth of the water column. In the model, the attenuated light ($\frac{dI}{dz}$ or $\frac{dI'}{dz}$) in both directions was added to the water column as a volumetric heat source (in a manner similar to that presented in Suárez et al. 2010).

[17] In addition to solar radiation attenuation in the water column, the fraction of the shortwave energy that is not reflected ($1 - R$) is absorbed at the bottom of the modeled column. This absorbed energy E_a (Eq. 9) is added to the bottommost cells of the model as a heat flux:

$$E_a = I_0(1 - A)(1 - R) \sum_{n=1}^7 f_n \exp(-\alpha_n z_{\text{max}}). \quad (9)$$

Numerical Methods

[18] The model was discretized into 14 rows and 165 columns (2310 model cells averaging $2.5 \text{ cm} \times 2.5 \text{ cm}$) and formulated in Fluent. The surface energy fluxes and absorption of shortwave radiation were coded in C++ and linked to Fluent as user-defined functions (Fluent, Inc. 2006). The governing equations (i.e., continuity, conservation of momentum, and conservation of energy) were evaluated using a first-order, implicit

Table 2 Light attenuation parameters for Devils Hole (based on Branco and Torgersen 2009).

Wavelength range (nm)	Fraction of incident light f_n	Attenuation rate α_n (m^{-1})
< 400 (ultraviolet)	0.046	1.772 (calibrated in this study)
400–700 (visible light)	0.430	1.772 (calibrated in this study)
700–910	0.214	2.92
910–950	0.020	20.4
950–1090	0.089	29.5
1090–1350	0.092	98.4
> 1350	0.109	2880

formulation in a pressure-based, segregated solver. Pressure and velocity were coupled using the SIMPLE (semi-implicit method for pressure linked equations) algorithm, which enforces conservation of mass through related corrections to velocity and pressure (Fluent, Inc. 2006). Pressures were interpolated using the PRESTO (pressure staggering option) algorithm, which uses a discrete continuity balance to compute the pressure on each face of the finite volume (Fluent, Inc. 2006). Momentum and energy were evaluated using a second-order upwind estimate. After convergence, residuals for the continuity, momentum, and energy equations were on the order 10^{-4} , 10^{-4} , and 10^{-8} , respectively.

Model Parameterization

[19] The model was calibrated against DTS data collected 23–24 June 2010. To allow the simulations of year-round temperatures, the model was driven by meteorological data collected from the permanent monitoring station maintained on-site by the National Park Service. Calibration parameters were limited to four poorly constrained processes: bottom reflectivity R ; shortwave attenuation rate α ; wind scaling factor w ; and neuston coefficient N . Other values were taken from literature (e.g., shortwave and longwave albedo) or from field observations (θ , t_0 , t_f , T_r).

[20] The calibration parameters α (the attenuation rate of shortwave radiation) and R (reflectivity of the bottom) affect only the periods of direct solar radiation, and the parameter N (relating to the neuston layer) exerts more influence in direct radiation than it does during the rest of the day. Because w (wind scaling) is the parameter that most affects the periods without direct solar exposure, a two-step calibration process was used; w was determined by examining the times during which the DTS cable was not exposed to direct radiation, and then the remaining three parameters were optimized in MATLAB by using a shuffled complex evolution (SCE) algorithm (Duan et al. 1993). The SCE method uses a combination of probabilistic and deterministic approaches to estimate a set of parameters that returns a global minimum for an objective function. In this case, the root mean squared error (RMSE; Eq. 10) of the difference between the recalibrated DTS temperatures (T_{n_obs}) and the simulated temperatures

(T_{n_sim}) over 24 h of simulation was minimized:

$$\text{RMSE} = \sqrt{\frac{1}{n} \sum_{i=1}^n (T_{n_sim} - T_{n_obs})^2}. \quad (10)$$

The RMSE was calculated at 150-s intervals throughout the first 24 h of the simulation as a measure of calibration. There were 63 DTS observations available at each time, but several had to be omitted due to the signal losses described in the Results section below. After removing unreliable data, the RMSE was based on 29,952 observations.

[21] The parameterized model was validated by comparing the distribution of the simulated temperatures and the temperature observations made from 1999 to 2001 at depths of 12 cm and 45 cm by Threlloff and Manning (2003). The model depth was set to the observed depths, and 24-h simulations were run for each depth. Simulations were driven with 2009 climatological data, adjusted via the delta change method (Gleick 1986; Arnell 1998) to match the mean June air temperatures recorded in 1999–2001. Histograms of Threlloff and Manning's data were compared with histograms of the simulated substrate temperatures at depths of 12 cm and 45 cm.

Sensitivity Analysis

[22] A sensitivity analysis was performed to examine the model parameterization and to evaluate the potential for climate change to affect this aquatic ecosystem. The model's sensitivity to a given calibration parameter was defined as the relative change in model RMSE that resulted from a change of 10% in that parameter (Westhoff et al. 2007). In addition to the calibration parameters, the model's sensitivity to climate drivers was also examined: simulations were performed with artificially elevated air temperatures (temperatures increased by 1–5 °C) and varying water depths ($d = d_{obs} \pm 0.035$ m, a 10% change in the average depth on the shelf).

Results

Field Data

[23] Calibrated DTS data had a mean temperature resolution of 0.16 °C (calculated as the RMSE of the cali-

bration sections) and a mean accuracy of ± 0.38 °C (the mean bias of the validation sections).

[24] The westernmost 12 m of cable in the bottom transect (corresponding to 120 cm of the shallow shelf) exhibited apparent calibration problems. Although the cable was not exposed to the air, DTS temperatures in this section were abnormally low when the air was cooler than the water column and abnormally high when the air was warmer than the water. Whereas the high temperatures could be explained by absorption of direct radiation at the substrate, there was no apparent mechanism to cause the abnormally cool temperatures. The reservoir below the shelf was a near-constant temperature that was warmer than the water column, so any cooling would occur from heat loss at the water surface. We would therefore expect the bottom to be warmer than the surface, and this was the case over the rest of the transect. An examination of the raw Raman spectra data showed that signal losses in this section of the cable were highly variable in space, and this variability made aligning the forward and reverse signals unreliable. Because of the uncertainty in the differential attenuation term of Eq. 1, the calibrated data from this section were extremely noisy—even when no direct radiation was striking on the cable (and therefore no reason for spatial variation), these data exhibited a standard deviation of 0.35 °C (more than twice the uncertainty), compared with 0.14 °C for the remainder of the cross section. Because of this issue, 11 observations were removed from each DTS trace; removal of these observations left 52 temperature observations in each time step.

[25] Following the data trimming, the DTS showed clear temporal (Fig. 4A) and spatial (Figs. 4B–E) variations in the observed temperatures. The temporal variations were small during the times Devils Hole was shaded, but temperature changes of 1 °C or more occurred quickly when the water surface was exposed to direct solar radiation and when that radiation ceased. Despite the fast cooling when direct insolation ends, the system did not continue to cool at night; the connection to the constant 33.5 °C reservoir below the shelf maintains nighttime water temperatures warmer than the ambient air (air temperatures dropped below 25 °C overnight).

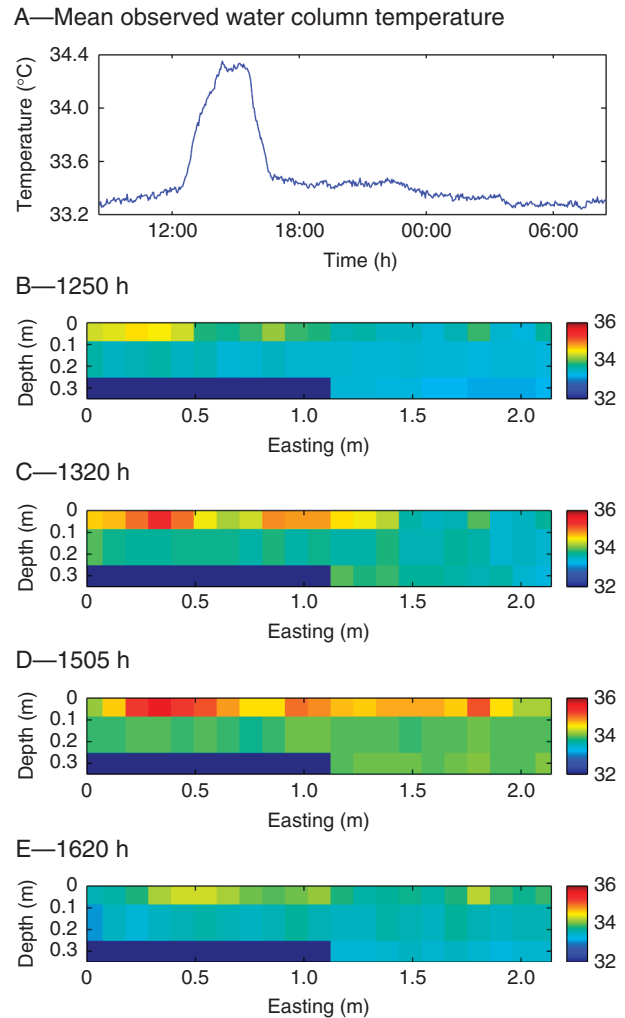


Fig. 4 Distributed temperature sensor observations. A — Mean water column temperatures exhibited a diel change. B–E — The cross-sectional temperature distributions exhibited spatial variations in temperature during periods of direct sunlight (23 June 2010, 1230 h–1620 h).

[26] The spatial variability of the DTS temperatures exceeded the temperature uncertainty only in the uppermost transect of the cable. For the 20-cm- and 35-cm-deep transects, the standard deviations of the 10 (bottom transect) or 21 (middle transect) observations were less than the temperature resolution of the DTS data; only the upper transect exhibited a spatial variation greater than the DTS uncertainty (Fig. 5). Because this difference was seen only in the uppermost layer, and because DTS cables in shallow systems have shown effects of direct solar radiation (Neilson et al. 2010;

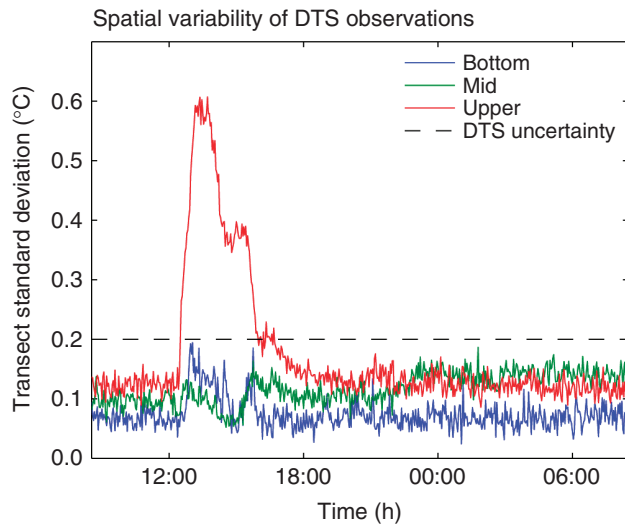


Fig. 5 Spatial variability in the distributed temperature sensor (DTS) observations, 23–24 June 2010.

Suárez et al. 2011a), we attribute this difference to absorption of direct radiation by the unshielded DTS cables themselves. The DTS temperatures in the upper transect were therefore corrected before comparing them with the modeled temperatures.

[27] DTS temperatures were corrected based on the spatial variations of observations in the upper transect. During direct radiation, there were typically two components to the transect; a warmer section where the cable was exposed to direct radiation, and a cooler section comprising the length of cable in the shade. *t*-tests showed that these components were almost always statistically distinct from one another (74 of 81 traces, $2.11 < t_{19} < 8.26$, $p < 0.05$). The mean difference between these two components over the duration of direct insolation was $0.89\text{ }^{\circ}\text{C}$. Before comparing the modeled water temperatures with the DTS observations, this difference was subtracted from the DTS observations made in direct sunlight (Fig. 6A).

Model Simulations

[28] The parameters used by the fully calibrated model are shown in Table 1. The model matched the corrected DTS observations with a mean RMSE of $0.19\text{ }^{\circ}\text{C}$ (within $0.05\text{ }^{\circ}\text{C}$ of the uncertainty of the calibrated DTS data). Observed temperatures ranged from $32.55\text{ }^{\circ}\text{C}$ to $35.19\text{ }^{\circ}\text{C}$, and the RMSE represents approximately 7% of this

range. As a quantitative metric, the Nash–Sutcliffe model efficiency (Nash and Sutcliffe 1970; Moriasi et al. 2007) was adapted to reflect the temperature:

$$E = 1 - \frac{\sum_{i=1}^{i_{\max}} (T_{\text{obs}}^i - T_m^i)^2}{\sum_{i=1}^{i_{\max}} (T_{\text{obs}}^i - \bar{T}_{\text{obs}})^2}, \quad (11)$$

where E is the Nash–Sutcliffe model efficiency, T_{obs}^i is the i th of i_{\max} temperature observations, T_m^i is the i th of i_{\max} modeled temperatures, and \bar{T}_{obs} is the mean of the observed temperatures. The model efficiency was 0.41, indicating that the model's predicted temperatures were substantially more accurate than using the daily mean temperature (A Nash–Sutcliffe value of 1 indicates a

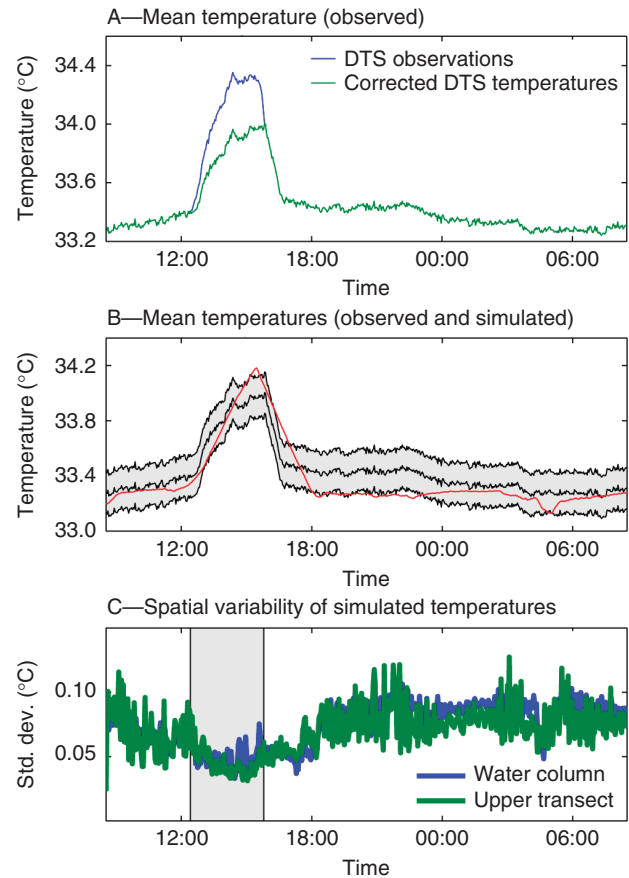


Fig. 6 A — Mean water column temperatures calculated from raw and radiation-corrected distributed temperature sensor (DTS) observations recorded 23–24 June 2010. B — Mean observed (heavy black line, with uncertainty shown in gray) and simulated (red) water column temperatures over the 24-h simulation. C — Spatial variability of the simulated temperatures, with the period of direct solar insolation shown in gray. Std. dev., standard deviation.

perfect match to observations; a value of 0 is equivalent to using the mean). The model performed slightly better during periods without direct solar radiation (mean RMSE during this time was 0.17 °C) and worse during direct insolation (mean RMSE was 0.29 °C during this period); this was not unexpected, since the absorption of direct solar radiation added considerable uncertainty to the midday DTS observations. The simulated water temperatures followed the same temporal pattern of heating and cooling that the DTS observations did (Fig. 6B), but the spatial variations seen in the upper transect of the DTS were not present in the model simulations (Fig. 6C).

[29] Although the simulated water temperatures were relatively uniform throughout the day, the convection patterns vary over time (Fig. 7). In the morning and evening, the vent (rightmost 15 cm of the bottom of the

simulation domain) influenced both the temperature and circulation of the water (Fig. 7A–B,H); warm water entered the system from the vent and generated a large counterclockwise convection cell, with a smaller cell controlling the circulation near the vent itself. When direct radiation falls on the shelf and is absorbed at the bottom of the water column (Fig. 7C–E), additional temperature gradients drive the convection. While the water column temperature was less than the temperature of the reservoir below the vent, the influence of both the vent and the radiation could be seen (Fig. 7C): the vent set up a small counterclockwise cell directly above it, and the differential heating created a larger clockwise cell to the west of the vent. As the water column temperature increased (Fig. 7D–E), the influence of the 33.5 °C vent lessened and mixing took the form of smaller, dynamic cells. With the cessation of

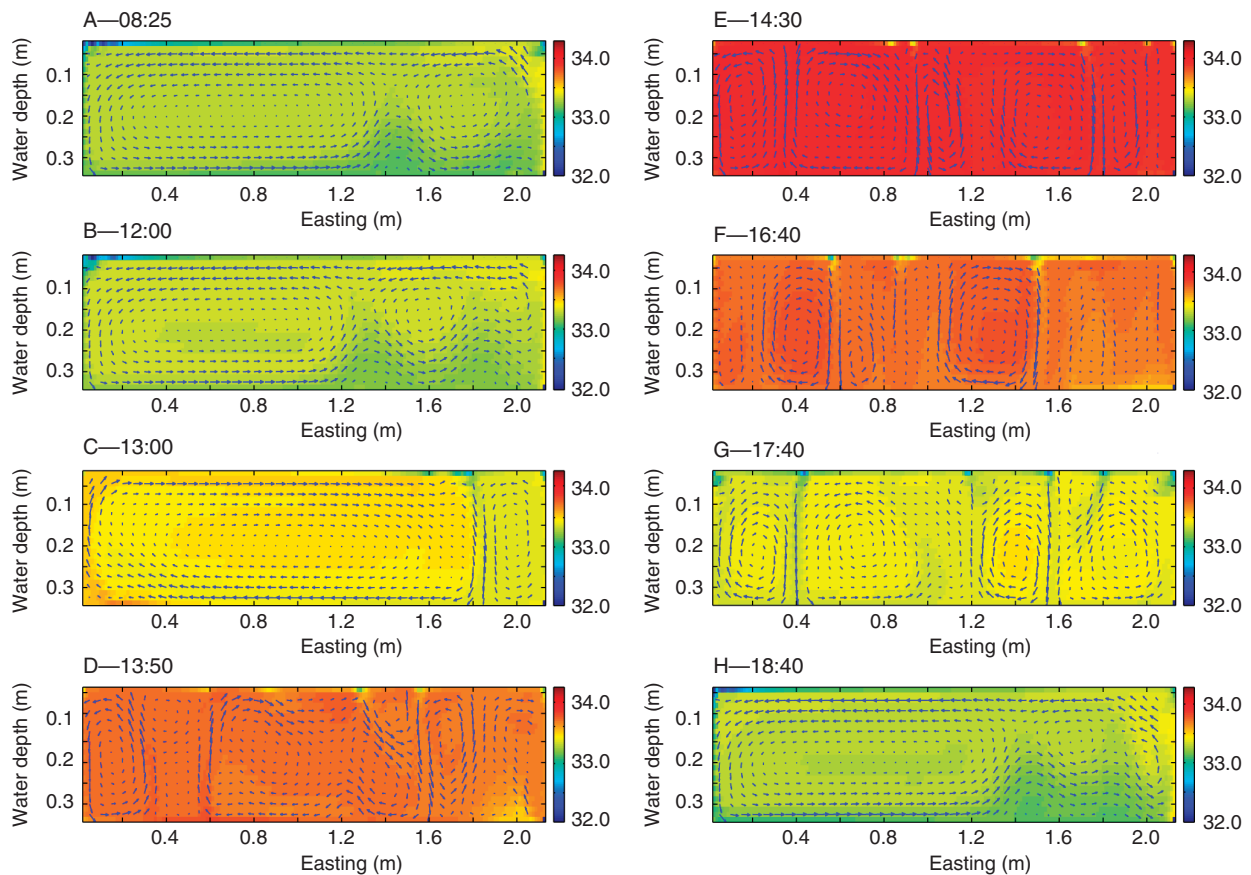


Fig. 7 Water temperatures and circulation patterns (indicated by vectors) predicted at different times over a 24-h simulation. A — stable nighttime circulation; B — after conductive and sensible warming; C — with spatially variable direct radiation; D — with spatially uniform direct radiation; E — daily peak temperature; F — cooling from the surface; G — reestablishing vent-driven convection; H — stable nighttime circulation pattern.

direct radiation (~ 1620 h), the system cooled primarily from the surface by latent and sensible heat fluxes. Water cooled at the surface plunged unpredictably to mix with the water below. While the water column was still warmer than the vent temperature of 33.5 °C (Fig. 7F), the vent exerted little influence; the vent began to form its own convection cell when the water temperature fell below 33.5 °C, even while cooling continued from the water surface (Fig. 7G). Within 2 h, the system returned to a vent-controlled convection pattern similar to the one observed before the onset of direct radiation (Fig. 7H). This pattern persisted until the onset of direct radiation on the following day.

Model Sensitivity

[30] The sensitivity of the model to the calibration parameters and the climate change drivers is described in Table 3. Of the calibration parameters, the model exhibited the greatest sensitivity to the attenuation rate of visible light and the least sensitivity to the wind scaling factor. However, the model's sensitivity to a 1 °C change in air temperature was approximately the same magnitude as its sensitivity to the calibration parameters, and its sensitivity to water depth was an order of magnitude greater than that.

Discussion

Field Data

[31] The uniform simulated temperatures support the idea that the spatial variability observed in the upper DTS transect was due primarily to direct radiation, and the corrected diel temperature changes observed in the field match cycles noted by previous researchers (Lyons 2005; Threlloff and Manning 2003). To evaluate

the 0.89 °C correction for direct exposure of the surface transect, we consider the theoretical model presented by Neilson et al. (2010) for estimating the impact of direct solar radiation on the cables:

$$\Delta T = \frac{q_{sw}}{2\bar{h}}, \quad (12)$$

where ΔT is the difference between the cable temperature and the water temperature, q_{sw} is the shortwave irradiance of the cable, and \bar{h} is the heat transfer coefficient between the cable and the water, a function of the thermal conductivity of the water, a characteristic length scale, and the Nusselt number Nu (the ratio of convective to conductive heat transfer across a boundary):

$$Nu = \begin{cases} C Re_D^m Pr^{1/3} & \text{for flow normal to the cable,} \\ 0.664 Re_L^{1/2} Pr^{1/3} & \text{for flow axial to the cable,} \end{cases} \quad (13)$$

where C and m are coefficients based on the Hilpert relationship (Incropera et al. 2007), Pr is the Prandtl number (the ratio of the diffusivity of momentum to the thermal diffusivity), and Re_D and Re_L are Reynolds numbers (the ratio of inertial to viscous forces) with length scales based on the cable diameter and the development of a thermal boundary layer, respectively. This model considers two cases: flow normal to the cable; and flow axial to the cable. Because the cable in this deployment was placed in overlapping spirals, we treat these two cases as end-members and expect the actual correction to fall somewhere between these values. Using a range of velocities between 0.005 and 0.01 m s⁻¹ (simulated velocities discussed below), axial and cross-flow length scales of 0.20 m and 0.001 m, respectively, and

Table 3 Sensitivity of the computational fluid dynamic model of Devils Hole to calibration parameters. Except for air temperature, sensitivity to a parameter is defined as the relative change in model root mean squared error (RMSE) resulting from a change of 10% in that parameter (Westhoff et al. 2007). Sensitivity to air temperature is defined as the relative change in RMSE resulting from a change in air temperature of ± 1 °C.

Parameter	Value	Units	Range	Sensitivity
Reflectivity of substrate (R)	0.476	Dimensionless	0.428–0.524	0.044
Neuston coefficient (N)	0.550	Dimensionless	0.505–0.605	0.034
Attenuation rate of shortwave light	1.772	m ⁻¹	1.595–1.949	0.093
Wind scaling parameter (w)	0.356	Dimensionless	0.320–0.392	0.027
Depth of water column	0.35	m	0.315–0.385	0.274
Mean air temperature	33.87	°C	32.87–34.87	0.047

an incident solar radiation of 1000 W m^{-2} (typical of the midday Mojave in June), we find values of ΔT ranging from 0.1°C (0.005 m s^{-1} cross flow) to 1.7°C (0.01 m s^{-1} axial flow). Since the 0.89°C correction described above falls well within this range, the temperature differences in the upper transect were most likely due to the greater absorption of solar radiation by the cable than by the adjacent water column.

Model Results and Validation

[32] Simulated velocities along the bottom of the model domain were low (the velocity along the bottom boundary never reached 0.01 m s^{-1}), making disturbance of the substrate unlikely. The dislodgment of algae, like sediment, typically occurs during infrequent, high-velocity turbulent flows (Hart and Finelli 1999). With a length scale of 1.94 m (the length of the physical boundary), Reynolds numbers along the shelf did not exceed 2.4×10^4 . For flow along a flat plate with an analogous length scale, the transition to turbulent flow occurs at $Re = 5 \times 10^5$ (Rubin and Atkinson 2001). Field observations of the shallow shelf match the simulations—the algae and substrate composition did not appear to move as a result of flowing water. The representation of the shallow shelf as a flat boundary was adequate for this model.

[33] Between 1999 and 2001, Threlhoff and Manning (2003) recorded substrate temperatures at different depths on the shallow shelf and reported monthly compiled temperatures with an uncertainty of 0.25°C . Their observations are compared with model results from the appropriate depths in Fig. 8. Threlhoff and Mannings's observations included 3 years of data (1999–2001) and incorporated both the variability of weather and the tidal cycles that influence water depth (depth of observations ranges from 42 to 48 cm and from 9 to 15 cm in Fig. 8, A and B, respectively). The observations thus include a few extreme points that the simulation does not. However, the observed and simulated histograms exhibit similar shapes and frequency distributions. Although the model is sensitive to water depth, these histograms indicate that this sensitivity is a feature of the ecosystem and not an artifact of the model.

[34] Previous investigations have reported water temperatures on the shallow shelf of Devils Hole (Table 4), although little information about the water depth, time of day, location, or accuracy and precision of historical observations is available. When we consider the variability in the observations, we note that the previously reported data, sparse though they are, fall within the same range as Threlhoff and Manning's (2003) observations.

Vulnerability to Climate Change

[35] The sensitivity analysis showed that the model is most sensitive to changes in water level and direct solar radiation, which are unlikely to be directly affected by climate change. Modest changes in air temperature (up to 1°C) led to negligible changes in the simulated water temperatures, but greater temperature increases were strongly linearly correlated with increases in both the peak daily temperature ($r = 0.98$) and the daily mean temperature ($r = 0.99$; Fig. 9E). To determine whether this pattern holds year round, an end-member winter simulation was run using the mean meteorological data from January 2010. In January, the sun angle is not high enough to allow any direct sunlight to reach the surface of Devils Hole, and heat transfer between the water column and the environment is a function of wind, air temperature, and humidity. In the winter simulations (Fig. 9B), increased air temperatures resulted in similar increases in both the mean and the peak water column temperatures; the daily mean temperature, however, remained $0.3\text{--}0.4^\circ\text{C}$ less than the summer mean temperatures.

[36] Because of the limited habitat, temperature and oxygen thresholds, and limited food supply, the Devils Hole pupfish is commonly thought to be extremely susceptible to the impacts of climate change. Shrode and Gerking (1977) show a sharp decline in *Cyprinodon* egg viability at the edge of the temperature threshold—in *C. n. nevadensis*, hatching success drops from almost 80% at 30°C to approximately 10% at 32°C . During the spring, reproduction in Devils Hole is encouraged by increases in both dissolved oxygen and food availability on the shallow shelf, but the annual peaks of dissolved oxygen, allochthonous inputs, or

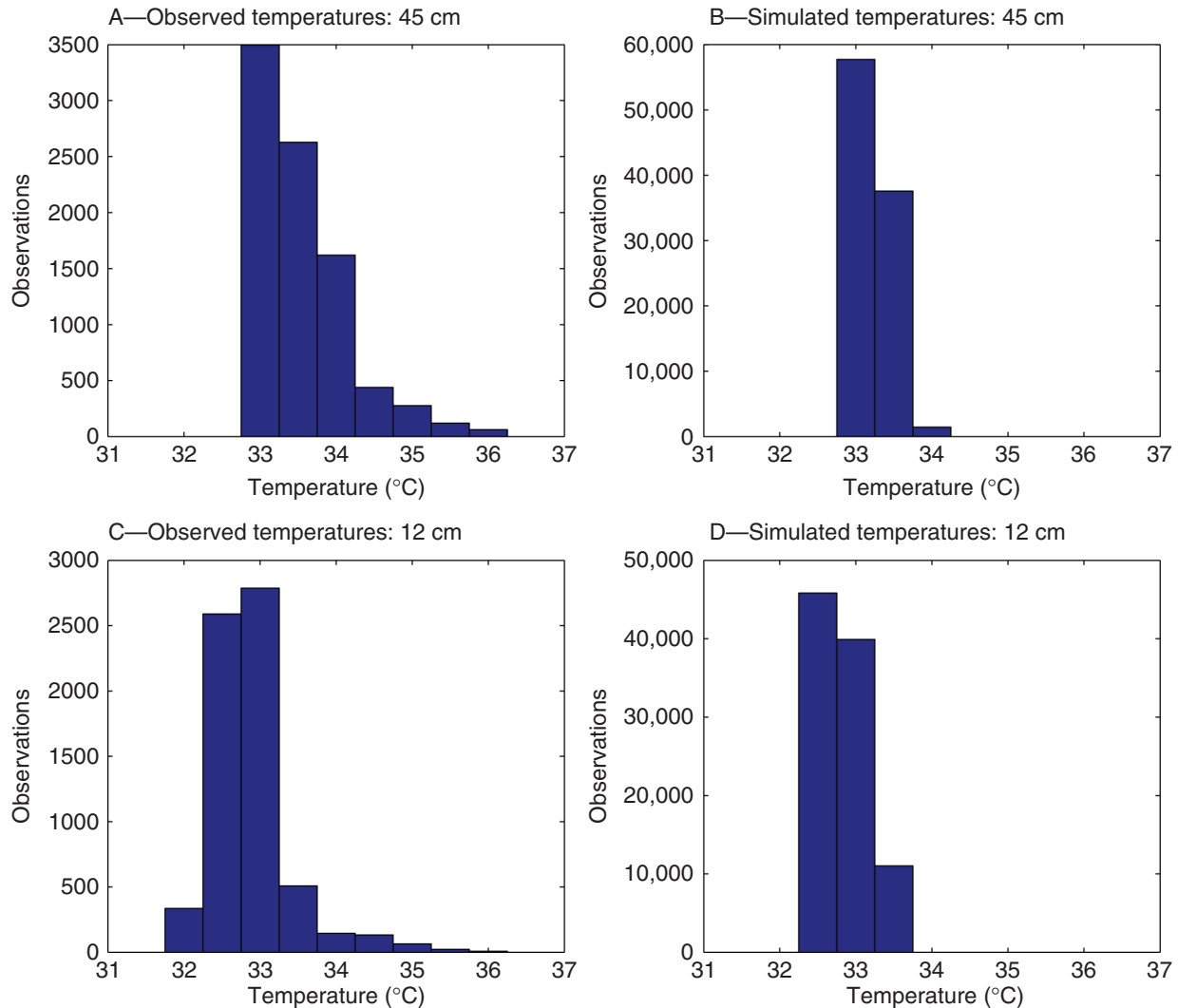


Fig. 8 Histograms of observed (A and C) and simulated (B and D) water temperatures at 45 cm (A and B) and 12 cm (C and D). Observed data are from Threlhoff and Manning (2003).

autochthonous production (Wilson and Blinn 2007) have historically occurred later in the year than the recruitment period. Based on the seasonal cycles of population, temperature, allochthonous carbon, and primary productivity, we posit that the peak daily water temperatures act as a control on the reproductive success and recruitment of *C. diabolis*. As with other *Cyprinodon* spp., small changes in these temperatures may inhibit or stop monthly recruitment (Shrode and Gerking 1977). Our model predicts a 0.1-°C increase in peak water temperature will result from an air temperature increase of just 1.6 °C. While global average temperatures are expected to rise by this amount

over the next century, temperatures in the southwestern United States have already increased approximately 1.5°C above the 1960–1979 historical baseline (Karl et al. 2009). Moreover, the model demonstrates that air temperature changes of that magnitude may cause observable changes in the water temperature on the shallow shelf. Mean water level in Devils Hole varies over time, but the post-1995 variation (0.625 ± 0.031 m below benchmark, $n = 5290$) is not significantly different from the 1980–1995 variation (0.624 ± 0.043 m below benchmark, $n = 5392$). Since water depth has not changed, the regional temperature changes between the mid-1970s and the present may

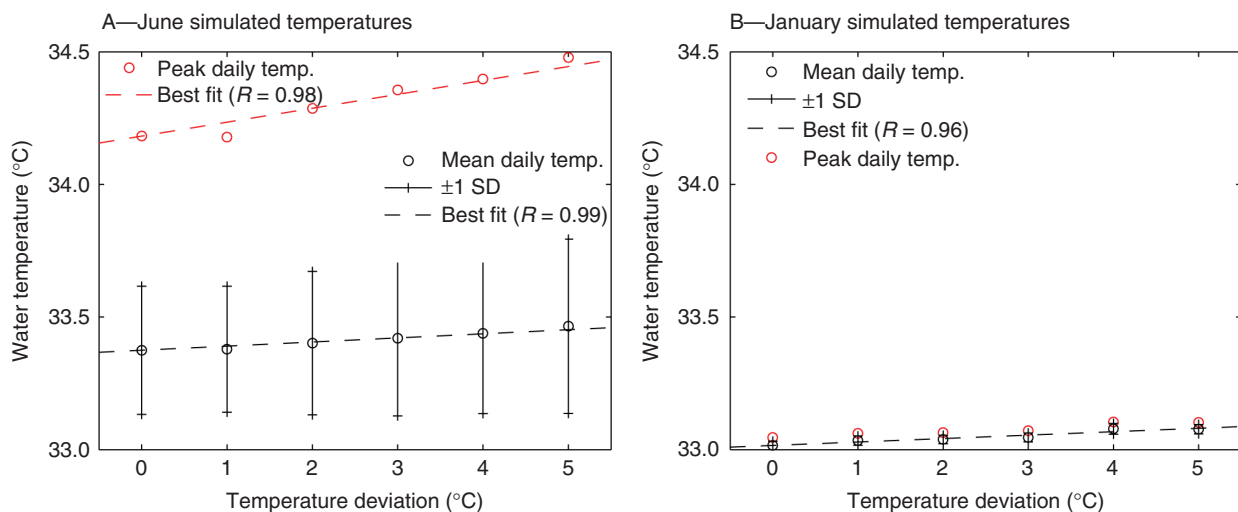
Table 4 Reported water temperatures in Devils Hole (based on Threlhoff and Manning 2003).

Date	Time (if known)	Temperature	Reference
March 1930	Unknown	33.9 °C (reported as 93 °F)	Wales 1930
Spring 1939	Unknown	33.5 °C	Sumner and Sargent 1940
1930–1947	Unknown	33.0 °C (mean of eight observations ranging from 32.8 to 33.9 °C)	Miller 1948
22 January 1953	Unknown	33.3 °C (reported as 92 °F)	Walker and Eakin 1963
1960	Unknown	33.4 °C	La Rivers 1962
9 December 1966	Unknown	33.3 °C (reported as 92 °F)	Naff 1973
December 1966	Unknown	33.5 °C	Dudley and Larson 1976
1967–1968	Unknown	33.4–34.0 °C	James 1969
April 1996	All day	32.1–33.8 °C	Gustafson and Deacon 1997
June 1996	All day	32.5–34.2 °C	Gustafson and Deacon 1997
May 1997	All day	31.0–36.0 °C	Gustafson and Deacon 1997
1999–2001	Three years of continuous observations	32.9 ± 0.6 °C ($\mu \pm \sigma$); 23.82–36.6 °C (full range)	Threlhoff and Manning 2003
23–24 June 2010	Continuous observations for 48 h	33.4 ± 0.25 °C ($\mu \pm \sigma$); 32.55–35.16 °C (full range)	Present study

have affected the reproductive success and recruitment of *C. diabolis*.

[37] Whereas current general circulation models (GCMs) project further temperature increases of 2–8 °C by 2099 (depending on the particular model and emissions scenario) in the southwestern United States (Karl et al. 2009), the gross temperature changes simulated by GCMs are typically reported on annual timescales. Because annual cycles of recruitment, food production, and water temperature in Devils Hole are seasonal, and because the climate changes are not evenly distributed throughout the year, further investigation into projected temperatures is necessary. The annual cycles of water

temperature, allochthonous carbon input, and primary productivity in Devils Hole will likely respond to climate changes in different ways. The anticipated changes in the temperature and hydrology of the region may affect the allochthonous carbon contributions, which comprise plant material, insects, feces, and detritus (Wilson and Blinn 2007), in different ways than they impact primary productivity (which is limited by solar exposure due to the physical structure of the system). Further research is necessary to assess the impacts of climate change on these processes and to explore potential management strategies to mitigate these impacts on the Devils Hole ecosystem.

**Fig. 9** Sensitivity of the Devils Hole system to changes in ambient air temperature. SD, standard deviation. A — Summer simulations. B — Winter simulations.

Significance to Aquatic Environments

[38] Desert areas are among those expected to be most affected by climate change (Karl et al. 2009), and desert aquatic ecosystems are not well understood or studied. Because Devils Hole and the population of Devils Hole pupfish respond very quickly to stresses, this ecosystem allows us to rapidly test hypotheses and validate models of ecological response to climate stressors. The computational fluid dynamic (CFD) model presented here simulates the physical response of the shallow water column of Devils Hole to daily meteorological cycles. Model results show that small increases in air temperature (i.e., changes on the order of those already observed in the southwestern United States) have the potential to raise the water temperatures on the shallow shelf of Devils Hole, influencing a critical component of the habitat of the endangered *C. diabolis*. In addition to acting as a possible control on pupfish recruitment, water temperatures also influence other ecologically important processes (e.g., biogeochemical cycling, dissolved oxygen). CFD-based predictions of thermal responses to climate change can be tested in the short term in settings like Devils Hole, but the results of such testing and the utility of climate-driven CFD modeling can be expanded to other ecosystems in other settings. The work presented here can be adapted to examine complex interactions of energy and ecology in other aquatic ecosystems.

[39] The spatial restrictions, proximity to environmental thresholds, and small population of pupfish combine to make Devils Hole a “canary in the global coal mine” (S. Hilyard, pers. comm., 2011). The response of Devils Hole to the changing climate may be used to guide our expectations of how analogous systems will respond; for example, Ash Meadows National Wildlife Refuge (in which Devils Hole is located) is home to three other warm-adapted endemic endangered fish species that share the climatic regime of Devils Hole (U.S. Fish and Wildlife Service 1990), and the habitats of coldwater fish are also threatened by thermal stresses associated with climate change (Eaton and Scheller 1996; Mohseni et al. 2003). Improved models and continued observations of Devils Hole, should provide data to evaluate and manage aquatic systems to mitigate these thermal impacts of climate change.

Acknowledgments The authors wish to thank the editors and two anonymous reviewers for their constructive criticism on this paper, as well as John Selker, Tom Torgersen, Michael Bower, Paul Barrett, and Gayton Scopetone for their help in this project. This work was funded by the U.S. National Park Service grant J8R07090002, the Nevada Department of Wildlife, the Death Valley Natural History Association, and National Science Foundation grant EAR-0930061.

Appendix: Surface Heat Flux

[A1] The net surface energy flux (Eq. 3) was calculated as a function of surface water temperature and the meteorological parameters measured onsite:

$$Q_{\text{surface}} = Q_e + Q_s + Q_l, \quad (\text{A1})$$

where Q_e represents the latent (evaporative) heat flux, Q_s the sensible heat flux, and Q_l the net longwave heat flux.

[A2] The latent heat flux (Eq. A2) was calculated as a function of forced convection (Q_{forced} , Eq. A3) and free or natural convection (Q_{free} , Eq. A4) (Adams et al. 1990). Because the neuston layer impedes evaporation from the water surface, the calculated evaporation was scaled according to the neuston parameter N :

$$Q_e = -(1 - N)\sqrt{Q_{\text{forced}}^2 + Q_{\text{free}}^2}, \quad (\text{A2})$$

$$Q_{\text{forced}} = 0.031U_2(e_{\text{sw}} - e_a), \quad (\text{A3})$$

$$Q_{\text{free}} = \begin{cases} 0.027(T_{\text{wv}} - T_{\text{av}})^{1/3}(e_{\text{sw}} - e_a) & \text{for } T_{\text{wv}} > T_a, \\ 0 & \text{for } T_{\text{wv}} \leq T_a, \end{cases} \quad (\text{A4})$$

$$e_{\text{sat}} = 2.1718 \times 10^{10} \exp\left(-\frac{4157}{T - 33.91}\right), \quad (\text{A5})$$

$$e_a = RH \cdot e_{\text{sat}}, \quad (\text{A6})$$

$$T_{\text{wv}} = \frac{T_w}{1 - 0.378e_{\text{sw}}P^{-1}}, \quad (\text{A7})$$

$$T_{\text{av}} = \frac{T_a}{1 - 0.378e_aP^{-1}}, \quad (\text{A8})$$

where U_2 is wind speed (m s^{-1}) 2 m above the water surface and e_{sw} and e_{sat} are the saturated vapor pressure (Pa) at the virtual temperature of the water surface at the air temperature, respectively. Both saturated vapor pressures are estimated using Eq. A5, in which T (K) is temperature (Brutsaert 1982). e_a is the actual vapor pressure (Eq. A6, in which RH is the relative humidity measured on site); and T_{wv} (Eq. A7) and T_{av} (Eq. A8) are the virtual temperatures (K) of the water surface and the air, respectively (Brutsaert 1982). In Eqs. A7 and A8, P is the atmospheric pressure (in the same units as e_a or e_{sw}).

[A3] The sensible heat flux Q_s (Eq. A9) is a function of wind speed and the temperature difference between the water surface (T_w) and the air (T_a) above it (Losordo and Piedrahita 1991):

$$Q_s = -1.5701 \cdot U_2(T_w - T_a). \quad (\text{A9})$$

[A4] The wind speeds observed onsite were measured at an elevation 3 m above the ridge overlooking the east side of Devils Hole, while the canyon walls obstructed wind flow and disrupted the near-surface boundary layer above the water surface. Because the above equations were formulated assuming a fully developed boundary layer, the observed wind speed is not considered a suitable model input; instead, this value was scaled as $U_2 = wU_3$, where U_2 is the value used in Eqs. A3 and A9, w is a scaling factor between 0 and 1 (the value of w was calibrated as described above), and U_3 is the observed wind speed 3 m above ground level.

[A5] The net longwave heat flux (Q_l) was the sum of the longwave radiation emitted by the water column (Q_l^w , Eq. A10; Rosenberry et al. 2007), the longwave emissions from the atmosphere (Q_l^a , Eq. A11; Henderson-Sellers 1986), and the emitted radiation from the canyon walls enclosing Devils Hole (Q_l^r , Eq. A12):

$$Q_l^w = -0.972\sigma T_w^4, \quad (\text{A10})$$

$$Q_l^a = (1 - al)\theta\epsilon_a\sigma T_a^4, \quad (\text{A11})$$

$$Q_l^r = 0.9(1 - \theta)\sigma T_r^4, \quad (\text{A12})$$

$$\begin{aligned} \epsilon_a = 0.84 - (0.1 - 9.973 \times 10^{-6} \epsilon_a)(1 - C) \\ + 3.491 \times 10^{-5} \epsilon_a \text{ for } C \leq 0.6. \end{aligned} \quad (\text{A13})$$

[A6] In these equations, σ is the Stefan-Boltzmann constant, the longwave surface albedo al of the water is assumed constant at 0.03 (Henderson-Sellers 1986), ϵ_a is the atmospheric emissivity (Eqs. 5–13, in which C is the fraction of cloud cover; Henderson-Sellers 1986), θ is a coefficient that represents the fraction of the sky directly visible to the water surface (i.e., not obstructed by the radiating canyon walls) (Westhoff et al. 2011), and T_r is the temperature of the canyon walls, assumed to be constant at the daily mean temperature.

References

- Adams, E., D. Cosler, and K. Helfrich. 1990. Evaporation from heated water bodies—predicting combined forced plus free convection. *Water Resour. Res.* **26**: 425–435. doi:10.1029/WR026i003p00425.
- Andersen, M. E., and J. E. Deacon. 2001. Population size of Devils Hole pupfish (*Cyprinodon diabolis*) correlates with water level. *Copeia* 2001 **1**: 224–228. doi:10.1643/0045-8511(2001)001[0224:PSODHP]2.0.CO;2.
- Arnell, N. W. 1998. Climate change and water resources in Britain. *Clim. Change.* **39**: 83–110. doi:10.1023/A:1005339412565.
- Baugh, T. M., and J. E. Deacon. 1983. Daily and yearly movement of the Devils Hole pupfish (*Cyprinodon diaboils*) Wales in Devils Hole, Nevada. *Great Basin Nat.* **43**(4): 592–596.
- Branco, B. F., and T. Torgersen. 2009. Predicting the onset of thermal stratification in shallow inland water bodies. *Aquat. Sci.* **71**: 65–79. doi:10.1007/s00027-009-8063-3.
- Brutsaert, W. 1982. *Evaporation into the Atmosphere: Theory, History, and Applications*. Springer. doi:10.1007/978-94-017-1497-6.
- Chernoff, B. 1985. Population dynamics of the Devils Hole pupfish. *Environ. Biol. Fish.*, **13**(2): 139–147. doi:10.1007/BF00002582.
- Duan, Q. Y., V. K. Gupta, and S. Sorooshian. 1993. Shuffled complex evolution approach for effective and efficient global minimization. *J. Optim. Theory Appl.* **76**: 501–521. doi:10.1007/BF00939380.
- Dudley, W. W., Jr., and J. D. Larson. 1976. Effect of irrigation pumping on desert pupfish habitats in Ash Meadows, Nye County, Nevada. *U.S. Geol. Surv. Prof. Pap.* **927**: 1–52.
- Eaton, J. G., and R. M. Scheller. 1996. Effects of climate warming on fish thermal habitat in streams of the United States. *Limnol. Oceanogr.* **41**: 1109–1115. doi:10.4319/lo.1996.41.5.1109.
- Fluent, Inc. 2006. *FLUENT 6.3 User's Guide*.
- Gleick, P. H. 1986. Methods for evaluating the regional hydrologic impacts of global climate changes. *J. Hydrol. (Amst.)*. **88**: 97–116. doi:10.1016/0022-1694(86)90199-X.
- Gustafson, E. S., and J. E. Deacon. 1997. Distribution of larval Devils Hole pupfish, *Cyprinodon diabolis*, in relation to dissolved oxygen concentration in Devils Hole. Final Report to the National Park Service, Contract 1443PH813095341. U.S. National Park Service.
- Hart, D. D., and C. M. Finelli. 1999. Physical-biological coupling in streams: The pervasive effects of flow on benthic organisms. *Annu. Rev. Ecol. Syst.* **30**: 363–395. doi:10.1146/annurev.ecolsys.30.1.363.
- Hausner, M. B., F. Suárez, K. E. Glander, N. C. van de Giesen, J. S. Selker, and S. W. Tyler. 2011. Calibrating single-ended fiber-optic Raman spectra distributed temperature sensing data. *Sensors (Basel)*. **11**: 10859–10879. doi:10.3390/s111110859.
- Hausner, M. B., K. P. Wilson, D. B. Gaines, and S. W. Tyler. 2012. Interpreting seasonal convective mixing in Devils Hole, Death Valley National Park, from temperature profiles observed by fiber-optic distributed temperature sensing. *Water Resour. Res.* **48**: W05513. doi:10.1029/2011WR010972.
- Henderson-Sellers, B. 1986. Calculating the surface energy balance for lake and reservoir modeling: A review. *Rev. Geophys.* **24**: 625–649. doi:10.1029/RG024i003p00625.
- Herbst, D. B., and D. W. Blinn. 2003. Devils Hole benthic invertebrate community dynamics: Distribution, seasonality, and production. Sierra Nevada Aquatic Research Laboratory report, 7 March. Sierra Nevada Aquatic Research Laboratory.
- Incropera, F. P., D. P. Dewitt, T. L. Bergman, and A. S. Lavine. 2007. *Fundamentals of Heat and Mass Transfer*. John Wiley.
- James, C. J. 1969. Aspects of the ecology of the Devils Hole pupfish (*Cyprinodon diabolis*) Wales. MS thesis, University of Nevada, Las Vegas.

- Karl, T. R., J. M. Melillo and T. C. Peterson [eds.]. 2009. Global Climate Change Impacts in the United States. Cambridge University Press.
- La Rivers, I. 1962. Fishes and fisheries of Nevada. Nevada Fish and Game Commission.
- Losordo, T., and R. Piedrahita. 1991. Modeling temperature variation and thermal stratification in shallow aquaculture ponds. *Ecol. Modell.* **54**: 189–226. doi:10.1016/0304-3800(91)90076-D.
- Lyons, L. T. 2005. Temporal and spatial variation in larval Devils Hole pupfish (*Cyprinodon diabolis*) abundance and associated microhabitat variables in Devils Hole, Nevada. MS thesis, Southern Oregon University.
- Miller, R. R. 1948. The Cyprinodont Fishes of the Death Valley System of Eastern California and Southwestern Nevada. Miscellaneous Publications of the Museum of Zoology **68**. Univ. of Michigan Press.
- Mohseni, O., H. G. Stefan, and J. G. Eaton. 2003. Global warming and potential changes in fish habitat in U.S. streams. *Clim. Change.* **59**: 389–409. doi:10.1023/A:1024847723344.
- Moriasi, D. N., J. G. Arnold, M. W. Van Liew, R. L. Bingner, R. D. Harmel, and T. L. Veith. 2007. Model evaluation guidelines for systematic quantification of accuracy in watershed simulations. *Trans. ASABE.* **50**: 885–900.
- Naff, R. L. 1973. Hydrogeology of the southern part of the Amargosa Desert in Nevada. MS thesis, University of Nevada Reno.
- Nash, J. E., and J. V. Sutcliffe. 1970. River flow forecasting through conceptual models part 1—a discussion of principles. *J. Hydrol. (Amst.)* **10**: 282–290. doi:10.1016/0022-1694(70)90255-6.
- Neilson, B. T., C. E. Hatch, H. Ban, and S. W. Tyler. 2010. Solar radiative heating of fiber-optic cables used to monitor temperatures in water. *Water Resour. Res.* **46**: W08540. doi:10.1029/2009WR008354.
- Riggs, A. C., and J. E. Deacon. 2002. Connectivity in desert aquatic ecosystems: The Devils Hole story. Paper presented at Spring-Fed Wetlands: Important Scientific and Cultural Resources of the Intermountain Region, 7–9 May 2002, Las Vegas, Nevada. DHS Publication 41210, available at http://www.dri.edu/images/stories/conferences_and_workshops/spring-fed-wetlands/spring-fed-wetlands-riggs-deacon.pdf.
- Rosenberry, D. O., T. C. Winter, D. C. Buso, and G. E. Likens. 2007. Comparison of 15 evaporation methods applied to a small mountain lake in the northeastern USA. *J. Hydrol. (Amst.)* **340**: 149–166. doi:10.1016/j.jhydrol.2007.03.018.
- Rubin, H., and J. Atkinson. 2001. Environmental Fluid Mechanics. CRC Press. doi:10.1201/9780203908495.
- Selker, J. S., et al. 2006. Distributed fiber-optic temperature sensing for hydrologic systems. *Water Resour. Res.* **42**: W12202. doi:10.1029/2006WR005326.
- Shrode, J., and S. Gerking. 1977. Effects of constant and fluctuating temperatures on reproductive performance of a desert pupfish (*Cyprinodon n. nevadensis*). *Physiol. Zool.* **50**: 1–10.
- Suárez, F., J. E. Aravena, M. B. Hausner, A. E. Childress, and S. W. Tyler. 2011a. Assessment of a vertical high-resolution distributed-temperature sensing system in a shallow thermohaline environment. *Hydrol. Earth Syst. Sci.* **15**: 1081–1093. doi:10.5194/hess-15-1081-2011.
- Suárez, F., M. B. Hausner, J. Dozier, J. S. Selker and S. W. Tyler. 2011b. Heat transfer in the environment: Development and use of fiber-optic distributed temperature sensing. pp. 611–636. In M. A. dos Santos Bernardes [ed.], *Developments in Heat Transfer*. Intech.
- Suárez, F., S. W. Tyler, and A. E. Childress. 2010. A fully coupled, transient, double-diffusive convective model for salt-gradient solar ponds. *Int. J. Heat Mass Trans.* **53**: 1718–1730. doi:10.1016/j.ijheatmasstransfer.2010.01.017.
- Sumner, F. B., and M. C. Sargent. 1940. Some observations on the physiology of warm spring fishes. *Ecology* **21**: 45–54. doi:10.2307/1930617.
- Szabo, B. J., P. T. Kolesar, A. C. Riggs, I. J. Winograd, and K. R. Ludwig. 1994. Paleoclimatic inferences from a 120,000-yr calcite record of water-table fluctuation in Browns Room of Devils Hole, Nevada. *Quaternary Res.* **41**: 59–69. doi:10.1006/qres.1994.1007.
- Threloff, D., and L. Manning. 2003. Thermal environment of the Devils Hole pupfish (*Cyprinodon diabolis*). Draft report. Death Valley National Park. U.S. National Park Service.
- Tyler, S. W., J. S. Selker, M. B. Hausner, C. E. Hatch, T. Torgersen, C. E. Thodal, and S. G. Schladow. 2009. Environmental temperature sensing using Raman spectra DTS fiber-optic methods. *Water Resour. Res.* **45**: W00D23. doi:10.1029/2008WR007052.
- U.S. Fish and Wildlife Service. 1990. Recovery plan for the endangered and threatened species of Ash Meadows, Nevada. U.S. Fish and Wildlife Service, Portland Oregon.
- van de Giesen, N., S. C. Steele-Dunne, J. Jansen, O. Hoes, M. B. Hausner, S. Tyler, and J. Selker. 2012. Double-ended calibration of fiber-optic Raman spectra distributed temperature sensing data. *Sensors (Basel)*. **12**: 5471–5485. doi:10.3390/s120505471.
- Wales, J. H. 1930. Biometrical studies of some races of cyprinodont fishes, from the Death Valley region, with description of *Cyprinodon diabolis*, n.s.p. *Copeia* **1930**: 61–70. doi:10.2307/1437054.
- Walker, G. E., and T. E. Eakin. 1963. Geology and Groundwater of Amargosa Desert, Nevada—California. Groundwater Resources Reconnaissance Series **14**. Nevada Department of Conservation and Natural Resources.
- Westhoff, M. C., M. N. Gooseff, T. A. Bogaard, and H. H. G. Savenije. 2011. Quantifying hyporheic exchange at high spatial resolu-

ution using natural temperature variations along a first-order stream. *Water Resour. Res.* **47**: W10508. doi:10.1029/2010WR009767.

Westhoff, M. C., H. H. G. Savenije, W. M. J. Luxemburg, G. S. Stelling, N. C. van de Giesen, J. S. Selker, L. Pfister, and S. Uhlenbrook. 2007. A distributed stream temperature model using high-resolution temperature observations. *Hydrol. Earth Syst. Sci.* **11**: 1469–1480. doi:10.5194/hess-11-1469-2007.

Wilcox, J. L. 2001. Small population evolution and conservation: Insights from Death Valley pupfish. PhD diss., University of Colorado.

Wilson, K. P., and D. W. Blinn. 2007. Food web structure, energetics, and importance of allochthonous carbon in a desert cavernous limnocrene: Devils Hole, Nevada. *West. N. Am. Naturalist.* **67**: 185–198. doi:10.3398/1527-0904(2007)67[185:FWSEAI]2.0.CO;2.

Received: 14 December 2012

Amended: 25 April 2013

Accepted: 14 June 2013